Predicting the filamentation of high-power beams and pulses without numerical integration: A nonlinear geometrical optics method

Nir Gavish[*] and Gadi Fibich
School of Mathematical Sciences, Tel Aviv University, Tel Aviv 69978, Israel

Luat T. Vuong and Alexander L. Gaeta
School of Applied and Engineering Physics, Cornell University, Ithaca, New York 14853, USA
(Received 26 June 2008; published 7 October 2008)

We present an analytic method for predicting the initial self-focusing dynamics of high-power beams and pulses. Using this method we study the filamentation pattern of a variety of input profiles, without solving partial differential equations. In particular, this method shows that in the anomalous regime, high-power pulses with temporal super-Gaussian profiles will split in time into two shorter pulses, and spherically symmetric pulses with super-Gaussian spatiotemporal profiles will evolve into a spatiotemporal shell.

PACS number(s): 42.65.Sf

I. INTRODUCTION

Nonlinear wave collapse is a phenomenon intrinsic to many areas of physics. In nonlinear optics, the intensity-dependent refractive index leads to self-focusing where a beam with input power greater than the critical power P_{cr} may undergo collapse [1].

In self-focusing experiments, it is observed that when the input beam power exceeds several critical powers, the transverse spatial beam profile breaks up into several filaments, a phenomenon known as multiple filamentation [2]. For many years, the only explanation for multiple filamentation, due to Bespalov and Talanov [3], has been that multiple filamentation is initiated by random noise in the input beam profile. Subsequently, it turned out that the modulation instability analysis of Bespalov and Talanov is only valid for very high input powers where $P=O(100\,P_{cr})$ [4]. At lower powers [e.g., $P=O(10\,P_{cr})$], noisy beams initially collapse as a single filament [5]. After collapse is arrested due to higher-order effects, the beams undergo a few focusing-defocusing cycles, at which point they typically break into multiple filaments, whose locations are dependent on noise.

Since noise is by definition random, the multiple filamentation patterns of noise-induced multiple filamentation are different from shot to shot. This constitutes a serious drawback in applications, in which precise localization is crucial. Therefore a method for predicting and controlling multiple filamentation is desired.

The first model for deterministic multiple filamentation was suggested by Fibich and Ilan [6,5], who showed theoretically that the deterministic breakup of cylindrical symmetry by a linear-polarization state can lead to deterministic multiple filamentation patterns. However, multiple filamentation due to vectorial effects has not been observed in experiments [7]. The reason for this is that in order for vectorial effects to lead to multiple filamentation, the beam radius should self-focus down to approximately two wavelengths. In experiments, however, self-focusing is arrested prior to

this stage, due to temporal or higher-order effects such as plasma. In subsequent research, deterministic multiple filamentation patterns (i.e., control of the number and location of the filaments) is achieved through a deterministic breakup of the cylindrical symmetry of the input pulse by inducing astigmatism [8,9] or ellipticity [10], applying amplitude or phase masks [9,11], propagating the beam through grids and slits [12–14], and also by shaping super-Gaussian input beams [15]. Each of the above methods induces a characteristic filamentation pattern by breaking the cylindrical symmetry of the input pulse. For example, filaments induced by ellipticity are distributed along the ellipse axes, whereas in the collapse of super-Gaussian input beams the filaments are distributed around a circle. These deterministic filamentation patterns are generally deduced via qualitative arguments, however, and not from a quantitative theory that is capable of predicting the number and locations of the filaments.

In [15], we presented a nonlinear geometrical optics (NGO) method for predicting the initial self-focusing dynamics of high-power ($P \gg P_{cr}$) input beams. The idea of the method is as follows. In this high-power regime, diffraction can be initially neglected and beam propagation is dictated by self-phase-modulation (SPM). Therefore the phase can be calculated analytically and used to solve the eikonal equation for the rays trajectories analytically. This method explained why high-power Gaussian input beams collapse to a single filament, while super-Gaussian input beams evolve into a ring (that subsequently breaks into a ring of filaments). These analytic results were in agreement with experimental multiple filamentation patterns produced by propagation in water [15].

In this study, we further improve the NGO method by calculating the beam amplitude along the rays. This allows us to predict the intensity distribution of the beam along its propagation, which is much more informative than the rays distribution. The numerical calculation of the rays trajectories and of the amplitude evolution involves solving linear ordinary differential equations along each ray. Because it is not necessary to solve the nonlinear Schrödinger equation (NLSE) or any other PDE, the computational costs are minimal. We show that the results of the NGO method are in

---

*nirgvsh@tau.ac.il; URL: www.tau.ac.il/~nirgvsh

excellent agreement with direct simulations of the NLSE, and are applicable for a variety of input beams and pulses.

The paper is organized as follows. In Sec. II we present the NGO method. In Sec. III we apply the NGO method to the NLSE in one spatial dimension and show that high-power super-Gaussian input beams ($\psi_0 = ce^{-x^{2m}}$, $m > 1$) will split into two beams, whereas Gaussian input beams ($\psi_0 = ce^{-x^2}$) will not split. In Sec. IV we consider the NLSE with one temporal dimension in the anomalous dispersion regime and show that high-power super-Gaussian pulses ($\psi_0 = ce^{-t^{2m}}$, $m > 1$) will split in time. In Sec. V we apply the NGO method to the NLSE in two spatial dimensions and show that when the input profile is square ($\psi_0 = ce^{-x^{2m}-y^{2m}}$, $m > 1$), the beam initially collapses into four filaments located at the corners of the square. In addition, we show that it is possible to analyze the filamentation patterns in two (or more) dimensions using "one-dimensional" "building blocks." For example, the filamentation dynamics of the square beam $\psi_0 = ce^{-x^4-y^4}$ can be explained by considering the dynamics of e^{-x^4} and e^{-y^4} separately. Indeed, since each component is a super-Gaussian, it would split to two components. Therefore the square input beam would split into four filaments. Similarly, in the case of the two-dimensional input beam $\psi_0 = ce^{-x^4}e^{-y^2}$, the x component is a super-Gaussian, hence it would split, while the y component is Gaussian and therefore would remain localized. Therefore this two-dimensional input beam would split into two filaments located on the y axis. In Sec. VI we show that a focusing lens does not affect the filamentation dynamics in a bulk Kerr medium and find the conditions under which a lens affects the filamentation dynamics in the one-dimensional case. In Sec. VII we show that the NGO method is robust to amplitude and phase noise. In Sec. VIII we apply the NGO method to the NLSE in three spatiotemporal dimensions in the anomalous dispersion regime and obtain several predictions for the filamentation patterns of high-power pulses. For example, we show that the input pulse $\psi_0 = ce^{-x^4-y^4-t^4}$ will initially split into eight spatiotemporal wave packets located on the vertices of a cube, and that the input pulse $\psi_0 = ce^{-r^4-t^4}$, where $r = \sqrt{x^2+y^2}$, will initially collapse into two shorter pulses, each of which is a spatial ring. Finally, in Sec. IX we compare the NGO method with the linear power partitioning (LPP) method of Roskey *et al.* [16] of predicting the filamentation pattern by solving the linear Schrödinger equation.

II. NONLINEAR GEOMETRICAL OPTICS (NGO) METHOD

In this section we present the nonlinear geometrical optics (NGO) method for analyzing the initial self-focusing dynamics of high-power solutions of the dimensional NLSE with general nonlinearity

$$2ik_0\psi_z(z,x,y) + \nabla_\perp^2\psi + k_0^2 F(|\psi|^2)\psi = 0, \quad \nabla_\perp^2 = \frac{\partial^2}{\partial x^2} + \frac{\partial^2}{\partial y^2},$$
(1a)

with the collimated initial condition

$$\psi_0(0,x,y) = \psi_0(x,y),$$
(1b)

where "high-power" means that initially the nonlinearity dominates over diffraction, i.e.,

$$\nabla_\perp^2\psi_0 \ll k_0^2 F(|\psi_0|^2)\psi_0.$$

These equations model a pure self-focusing Kerr nonlinearity ($F = \frac{4n_2}{n_0}|\psi|^2$), a cubic-quintic nonlinearity, nonlinear saturation, a photorefractive nonlinearity, etc. The NGO method was first introduced in [15], and is further improved here.

Our starting point is the dimensional nonlinear Helmholtz equation (NLH)

$$\nabla^2 E(z,x,y) + k^2 E = 0, \quad k^2 = k_0^2[1 + F(|E|^2)],$$
(2)

where $\nabla^2 = \partial_{xx} + \partial_{yy} + \partial_{zz}$. Since $k_0 \gg 1$, we can look for solutions of the form

$$E(z,x,y) = A(z,x,y)e^{ik_0 S_E(z,x,y)}.$$
(3)

Substitution of Eq. (3) into the NLH equation (2) and balancing the $O(k_0^2)$ terms and $O(k_0)$ terms gives the *eikonal equation*

$$\boldsymbol{\nabla} S_E \cdot \boldsymbol{\nabla} S_E = 1 + F(A^2),$$
(4)

and the *transport equation*

$$2\,\boldsymbol{\nabla} S_E \cdot \boldsymbol{\nabla} A + A\boldsymbol{\nabla}^2 S_E = 0,$$
(5)

respectively.

Typically, the eikonal equation is solved using the method of characteristics (rays). Here, following [15], we take a different approach. We recall that the NLSE (1a) is derived from the NLH equation (2) by substituting $E(z,x,y) = \psi(z,x,y)e^{ik_0 z}$ and applying the paraxial approximation. Therefore, we consider NLSE solutions of the form

$$\psi(z,x,y) = A(z,x,y)e^{ik_0 S_\psi},$$

where

$$S_\psi = S_E - z.$$
(6)

In the case of high-power input beams, to leading order, the NLSE (1a) reduces to

$$i\psi_z(z,x,y) + \frac{k_0}{2}F(|\psi|^2)\psi = 0.$$
(7)

The (exact) solution of Eq. (7) is given by $\psi = \psi_0(x,y)e^{ik_0 S_\psi}$ where

$$S_\psi(z,x,y) = \frac{1}{2}F(|\psi_0|^2)z.$$
(8)

The eikonal equation implies that the rays are parallel to ∇S_E. Therefore the equation for the trajectories of the rays $\mathbf{x}(\sigma) = [x(\sigma), y(\sigma), z(\sigma)]$ is

$$\frac{d\mathbf{x}(\sigma)}{d\sigma} = \nabla S_E(\mathbf{x}(\sigma)),$$
(9)

where σ is the parameter of the ray. In addition, from Eqs. (6), (8), and (9) it follows that
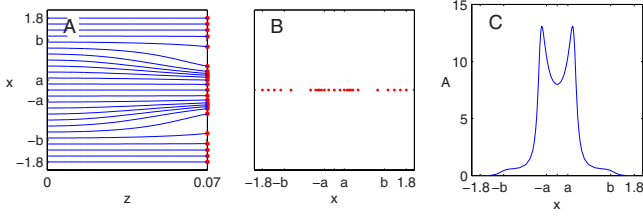
FIG. 1. (Color online) NGO predictions for the solution of the one-dimensional cubic NLSE with the super-Gaussian input beam $\psi_0 = 8e^{-x^4}$. (a) Trajectory of the rays. (b) Location of the rays at $z=0.07$. (c) Amplitude distribution at $z=0.07$.

$$\frac{dz(\sigma)}{d\sigma} = \frac{\partial}{\partial z}S_E \approx 1 + \frac{\partial}{\partial z}S_\psi \approx 1 + \frac{1}{2}F(|\psi_0|^2). \qquad (10)$$

Since even for high-power input beams $F(|\psi_0|^2) \ll 1$, it follows that $\frac{dz}{d\sigma} \approx 1$, hence $z \approx \sigma$. Therefore Eq. (9) reduces to

$$\frac{d}{dz}(x(z),y(z)) = \left(\frac{\partial}{\partial x}, \frac{\partial}{\partial y}\right) S_\psi(x(z),y(z),z), \qquad (11)$$

where S_ψ is given by Eq. (8).

In what follows, we will apply the NGO method to the dimensionless NLSE

$$i\psi_z(z,x,y) + \nabla_\perp^2\psi + F(|\psi|^2)\psi = 0 \qquad (12)$$

in the high power regime where $F(|\psi|^2)\psi \gg \nabla_\perp^2\psi$. In this case, the equation for the trajectories of the rays is given by

$$\frac{d}{dz}(x(z),y(z)) = 2\left(\frac{\partial}{\partial x}, \frac{\partial}{\partial y}\right) S_\psi(x(z),y(z),z), \qquad (13)$$

where

$$S_\psi(x(z),y(z),z) = F(|\psi_0(x,y)|^2)z, \qquad (14)$$

see Appendix A.

To illustrate this ray part of the NGO method, we consider the one-dimensional, dimensionless NLSE with Kerr (cubic) nonlinearity

$$i\psi_z(z,x) + \psi_{xx} + |\psi|^2\psi = 0, \qquad (15)$$

with a collimated super-Gaussian input beam

$$\psi_0 = 8e^{-x^4}. \qquad (16)$$

By Eq. (13), the corresponding equation for the trajectories of the rays is approximated as

$$\frac{dx(z)}{dz} = 2 \times 8^2 z \frac{\partial}{\partial x}e^{-2x^4(z)}. \qquad (17)$$

In Fig. 1(a) we plot the rays that are calculated from Eq. (17). In this example, rays that originate from $0.25 \approx a < |x| < b \approx 1.4$ bend toward the center and concentrate near $x = \pm a$. In contrast, rays originating at $|x| < a$ and from $|x| > b$ remain essentially parallel. Therefore we conclude that the input beam splits into two filaments centered at $x \approx \pm a$.

In the above analysis we implicitly assumed that regions where more rays are concentrated correspond to regions of higher intensity. Thus the two regions near $x \approx \pm a$ with high

density of rays were interpreted as two filaments. The problem with this approach is that it does not distinguish between the rays that originate from high intensity regions and those that originate from low intensity regions. For example, consider Fig. 1(b), where we plot the location of the rays at $z = 0.07$. While this plot shows the two spikes at $\pm a$, it also shows additional minor bumps at the wings of the beam.

In order to improve the quality of the graphical representation, we now extend the method beyond what was done in [15] and compute the evolution of the amplitude A along each ray. To do that for the dimensional NLSE (1a), we solve the *transport equation* (5) using the method of characteristics, i.e.,

$$\frac{d}{d\sigma}A(\mathbf{x}(\sigma)) = -\frac{1}{2}A(\mathbf{x}(\sigma))\nabla^2 S_E(x(\sigma)),$$

where $\mathbf{x}(\sigma)$ was already calculated from Eq. (9). From Eqs. (6) and (8) it follows that $\frac{\partial^2}{\partial z^2}S_E = 0$. Since, in addition, $z \approx \sigma$, the transport equation can be approximated with

$$\frac{d}{dz}A(x(z),y(z)) = -\frac{1}{2}A(x(z),y(z))\nabla_\perp^2 S_\psi(z,x(z),y(z)),$$
$$(18)$$

where S_ψ is given by Eq. (8). Similarly, the approximate transport equation for the dimensionless NLSE (12) is given by

$$\frac{d}{dz}A(x(z),y(z)) = -A(x(z),y(z))\nabla_\perp^2 S_\psi(z,x(z),y(z)),$$
$$(19)$$

where S_ψ is given by Eq. (14), see Appendix A.

In Fig. 1(c) we use this approach to calculate the amplitude distribution at $z = 0.07$, which corresponds to the rays distribution in Fig. 1(b). To do that we solve

$$\frac{d}{dz}A(x(z)) = -8^2 z A(x(z))\frac{\partial^2}{\partial x^2}e^{-2x^4}, \qquad (20)$$

where $x(z)$ was already calculated from Eq. (17). This representation clearly shows that the input beam splits into two filaments at $x = \pm a$, with no minor bumps at the wings of the beam, as is confirmed by solving the NLSE directly, see Fig. 4(c). Therefore the amplitude representation [Fig. 1(c)] is both cleaner and more informative than the ray representation [Fig. 1(b)].

The generalization of the NGO method to the multidimensional case is straightforward. For example, consider the two-dimensional, dimensionless NLSE with Kerr (cubic) nonlinearity

$$i\psi_z(z,x,y) + \psi_{xx} + \psi_{yy} + |\psi|^2\psi = 0, \qquad (21)$$

with a collimated square input beam of the form

$$\psi_0 = 6.55e^{-x^4-y^4}.$$

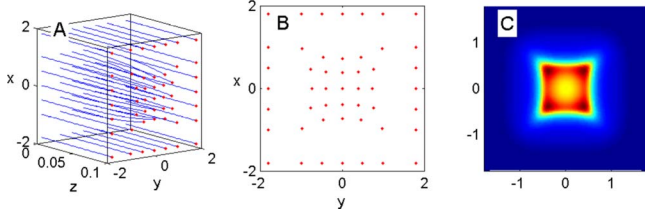In this case, the trajectories of the rays are calculated from Eq. (13), i.e.,

FIG. 2. (Color online) NGO predictions for the solution of the two-dimensional cubic NLSE with the input beam $\psi_0 = 6.55 e^{-x^4 - y^4}$. (a) Trajectory of the rays. (b) Location of the rays at $z = 0.1$. (c) Amplitude distribution at $z = 0.1$.

$$\frac{d}{dz}(x(z), y(z)) = 2 \times 6.55^2 z \left(\frac{\partial}{\partial x}, \frac{\partial}{\partial y} \right) e^{-2x^4 - 2y^4},$$

see Fig. 2(a). At any distance we can plot the location of rays in the (x, y) plane, see Fig. 2(b). However, as in the one-dimensional case, the location of the rays does not always provide a clear description of the beam profile. For example, in Fig. 2(b) it looks as though at $z = 0.1$ the beam is flat-topped at the center. To find the amplitude distribution at $z = 0.1$ we solve the dimensionless transport equation (19), i.e.,

$$\frac{d}{dz} A(z) = 6.55^2 z A(z) \nabla_\perp^2 e^{-2x^4 - 2y^4}.$$

The amplitude distribution shows that the beam evolved into four filaments located at the corners of a square, see Fig. 2(c), as is confirmed by solving the two-dimensional NLSE (21), see Fig. 11(b).

The generalization of the NGO method to the three-dimensional NLSE is identical and is demonstrated in Sec. VIII.

In summary, the nonlinear geometrical optics method for the dimensionless NLSE

$$i\psi_z(z, x, y) + \psi_{xx} + \psi_{yy} + F(|\psi|^2)\psi = 0,$$

is as follows:

(1) Choose starting points (x_i, y_j) for the rays at $z = 0$.

(2) For each ray, find its trajectory and amplitude by solving

$$\frac{d}{dz}(x(z), y(z), A(z)) = 2\left(\frac{\partial}{\partial x}, \frac{\partial}{\partial y}, -\frac{1}{2} A \nabla_\perp^2 \right) S_\psi(z, x(z), y(z)),$$

(22a)

where

$$S_\psi(z, x, y) = F(|\psi_0(x(z), y(z))|^2)z, \quad (22b)$$

with the initial condition

$$(x(0), y(0), A(0)) = (x_i, y_j, |\psi_0(x_i, y_j)|).$$

We emphasize that the NGO method does not require solving the NLSE or any other PDE, but only linear ODEs for each ray. Implementation of the method is, therefore, very simple and requires only a few lines of code in MATLAB, see Appendix B.
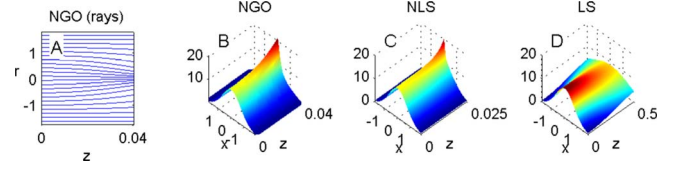

FIG. 3. (Color online) Solution of the one-dimensional cubic NLSE with a Gaussian input beam $\psi_0 = c e^{-x^2}$ with $c \approx 8.93$. (a) NGO prediction for the ray trajectories. (b) NGO prediction for the amplitude. (c) NLSE solution. (d) Linear Schrödinger solution.

Limitations of the NGO method

In the NGO method we consider the effects of the changes in the phase on the amplitude, but ignore the changes in the amplitude that occur due to the phase variations, see Eqs. (8) and (18). In the NLSE model, however, once the beam starts to focus, the amplitude increases at the region of focus. As a result, the nonlinear self-phase modulation effects become stronger and the collapse is further accelerated. Because the NGO method neglects this feedback effect, filamentation in the NGO approximation occurs at longer propagation distance as compared to that in the NLSE model.

For the same reason, the NGO method cannot successfully predict the dynamics that occurs after the beam starts to focus and to gain amplitude. This is because at this stage, the effects of the changes in the amplitude on the phase, which are neglected by the NGO method, start to become significant. Therefore the NGO method successfully predicts the initial filamentation pattern of high-power input beams, but cannot be used to study the subsequent filamentation dynamics that may occur.

III. ONE SPATIAL DIMENSION

Consider the one-dimensional NLSE

$$i\psi_z(z, x) + \psi_{xx} + |\psi|^2\psi = 0, \quad (23)$$

with a collimated input beam of the form

$$\psi_0 = c e^{-x^{2m}}, \quad (24)$$

where c is sufficiently large so that $|\psi_0|^2\psi_0 \gg (\psi_0)_{xx}$. For example, in what follows, the value of c is chosen so that $\int |\psi_0|^2 dx = 200$. In this case, by Eq. (22), the equation for the trajectories and amplitude of the rays is given by

$$\frac{d}{dz}(x(z), A(z)) = 2c^2 z \left(\frac{\partial}{\partial x}, -\frac{1}{2} A \frac{\partial}{\partial x^2} \right) e^{-2x^{2m}}. \quad (25)$$

When $m = 1$ (Gaussian input beam) the NGO ray analysis shows that all the rays concentrate towards $x = 0$, suggesting that the beam localizes to a single peak at $x = 0$, see Fig. 3(a). This is also observed in Fig. 3(b), where we plot the NGO prediction for the amplitude. To confirm this NGO prediction, we solve the one-dimensional NLSE (23), and find that, indeed, the solution localizes into a single filament at $x = 0$, see Fig. 3(c). As expected, the filamentation distance of the NLSE solution is shorter than the NGO prediction.

FIG. 4. (Color online) Same as Fig. 3 for the input beam $\psi_0 = ce^{-x^4}$ with $c \approx 8.09$.
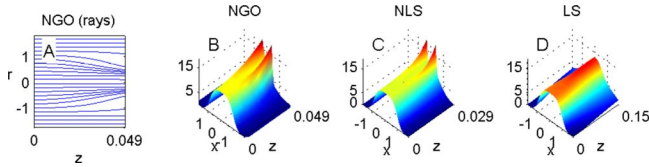

FIG. 5. (Color online) Same as Fig. 3 for the input beam $\psi_0 = ce^{-x^8}$ with $c \approx 8.09$.

In Fig. 4 we consider the case $m=2$ (super-Gaussian input beam), which models propagation through a soft aperture. In this case, the input beam is characterized by sharp gradients for $0.25 \approx a < |x| < b \approx 1.4$, and is essentially constant elsewhere. Therefore rays that originate from $a < |x| < b$ bend toward the center and concentrate near $x = \pm a$. In contrast, rays originating at $|x| < a$ and $|x| > b$ remain essentially parallel. Therefore the input beam splits into two beams which are localized around $x = \pm a$, see Fig. 4(a). Similar dynamics is evident in Fig. 4(b), where we plot the amplitude distribution using the NGO method. In Fig. 4(c) we confirm that, indeed, the corresponding NLSE solution splits into two filaments around $x = \pm a$. As expected, the filamentation distance of the NLSE solution is shorter than the one predicted by the NGO method.

In Fig. 5 we consider the case $m=4$ (super-Gaussian input beam), which models propagation through a hard aperture. As in the case of a soft aperture, rays that originate from $a < |x| < b$ bend toward the center and concentrate near $x = \pm a$. In contrast, rays originating at $|x| < a$ and $|x| > b$ remain essentially parallel. Therefore the input beam splits into two beams that are localized around $x = \pm a$, see Figs. 5(a) and 5(b). This NGO prediction is confirmed in simulations of the NLSE, see Fig. 5(c).

The NGO ray analysis, thus, shows that:

Observation III.1. Any one-dimensional super-Gaussian input beam with $m > 1$, whose power is sufficiently high so that initially the Kerr nonlinearity dominates over diffraction, will split into two beams.

Proof. We prove this observation by showing that rays originating around $x=0$ and far away from the beam center remain parallel, while rays originating between these regions bend toward the center. Indeed, by Eq. (25)

$$\frac{dx}{dz} = -8mc^2 x^{2m-1} e^{-2x^{2m}z}.$$

Therefore, far away from the beam center, $\frac{dx}{dz} \ll 1$, hence the rays are essentially parallel. Similarly, around $x=0$,

$$\frac{dx}{dz} = -8mc^2 x^{2m-1} z.$$

Therefore for $m > 1$ and for $x \ll 1$, $dx/dz \ll 1$ and the rays are essentially parallel. Finally, between the two regions [i.e., when $x = O(1)$], $dx/dz \approx -8mc^2 x^{2m-1}$. Therefore the rays in this region are not parallel, but rather bend towards the center. ∎
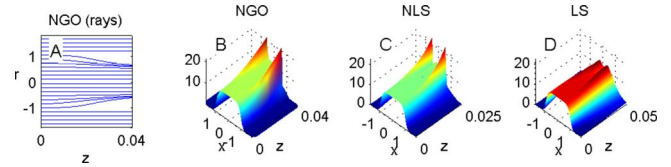
Of course, if m is only slightly larger than 1, then this effect would be weaker, hence the beam split would only be observed at higher input powers and over longer propagation distances.

It is well-known that super-Gaussian input beams can also split into two beams due to diffraction. In order to check whether diffraction could produce the filamentation patterns in Figs. 3–5, we solve the linear Schrödinger equation with the same input beams. In the case of a Gaussian input beam, linear effects result in broadening of the beam [Fig. 3(d)]. In the case of a soft aperture super-Gaussian input beam, diffraction results in minor initial localization of the beam toward one peak [Fig. 4(d)]. Only in the case of a hard aperture super-Gaussian input beam [Fig. 5(d)], the beam splits into two peaks. Therefore

Observation III.2. The linear Schrödinger equation predicts the initial filamentation dynamics of high power beams only when the input beam propagates through hard apertures, (i.e., has strong initial gradients).

Moreover, the linear model predicts that the splitting occurs as the beam diffracts, while in the NLSE the splitting occurs as the two filaments self-focus, a characteristic that is preserved in the NGO approximation.

Neither the NGO method, nor the linear model accurately predict the filamentation distance in the NLSE model. However, in the NGO method the predicted filamentation distance is always somewhat larger than the NLSE filamentation distance. In contrast, the filamentation distance in the linear model is independent of the input power. Therefore, unlike the NGO method, the linear model does not capture the decrease in the filamentation distance as the input power increases.

IV. ONE TEMPORAL DIMENSION

Consider the dimensionless one-dimensional NLSE with anomalous dispersion

$$i\psi_z(z,t) + \psi_{tt} + |\psi|^2 \psi = 0, \qquad (26)$$

with an input pulse of the form

$$\psi_0 = ce^{-t^{2m}},$$

where c is large enough so that $|\psi_0|^2 \psi_0 \gg (\psi_0)_{tt}$. Although this equation is not derived from the nonlinear Helmholtz equation (2), it can still be analyzed using the NGO method. This is because, up to the change $x \leftrightarrow t$, Eq. (26) is identical to Eq. (15). Therefore all the results of Sec. III (e.g., Figs. 3–5) are valid for this case as well. In particular,

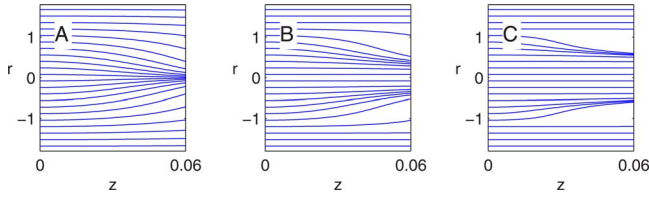*Observation IV.1.* In the anomalous regime, any temporal

FIG. 6. (Color online) NGO prediction for the ray trajectories of two-dimensional cubic NLSE with the radially symmetric input beam $\psi_0 = ce^{-r^{2m}}$. (a) $m=1$, $c=7.97$. (b) $m=2$, $c=7.12$. (c) $m=4$, $c=6.46$.

super-Gaussian pulses with $m>1$, whose power is sufficiently high so that initially the Kerr nonlinearity dominates over dispersion, will split in time into two shorter pulses.

Note, in addition, that the temporally split pulses are considerably shorter than the duration of the initial super-Gaussian pulse.

V. TWO SPATIAL DIMENSIONS

We now consider the filamentation dynamics of high-powered solutions of the two-dimensional NLSE

$$i\psi_z(z,x,y) + \psi_{xx} + \psi_{yy} + |\psi|^2\psi = 0. \tag{27}$$

A. Radially symmetric beams

We first consider the two-dimensional NLSE (27) with radially symmetric input beams

$$\psi_0 = ce^{-r^{2m}}, \quad r = \sqrt{x^2 + y^2}, \tag{28}$$

where c is sufficiently large such that $|\psi_0|^2\psi_0 \gg \nabla_\perp^2\psi_0$. In this case, by Eq. (22), the equation for the trajectories of the rays is given by

$$\frac{dr(z)}{dz} = 2c^2 z \frac{\partial}{\partial r} e^{-2r^{2m}}. \tag{29}$$

Therefore, up to the change $r \leftrightarrow x$, this is the same equation as the equation for the rays in the one-dimensional case, see Eq. (25). Note, however, that a beam split in the (x,z) plane is equivalent to a ring formation in the (r,z) plane. Therefore

Observation V.1. Any two-dimensional radially symmetric super-Gaussian input beam with $m>1$, whose power is sufficiently high so that initially the Kerr nonlinearity dominates over diffraction, will initially evolve into a ring.

Indeed, in Figs 6(a)–6(c) we plot the NGO prediction for

the ray trajectories for $m=1,2$, and 4, where c is chosen such that $2\pi\int_0^\infty |\psi_0|^2 r\,dr = 100$. Note that the ray trajectories in Figs 6(a)–6(c) are identical to the ray trajectories in Figs 3(a), 4(a), and 5(a), respectively. However, the interpretation of these figures is different. For $m=1$ the beam localizes to a single peak at $r=0$, see Fig. 6(a), while for $m=2$ and 4 the beam evolves into a ring, see Figs. 6(b) and 6(c).

By Eq. (22), the NGO prediction for the amplitude is given by

$$\frac{dA(z)}{dz} = -c^2 z A(z)\left[\frac{\partial}{\partial r^2} + \frac{1}{r}\frac{\partial}{\partial r}\right] e^{-2r^{2m}}. \tag{30}$$

Hence the equation for the amplitude is similar, but not identical, to the one in the one-dimensional case, see Eq. (25). In Fig. 7(a) we plot the NGO prediction for the amplitude distribution for the case $m=1$ and observe that the beam localized to a single peak at $r=0$, as was already predicted from the NGO ray analysis. This NGO prediction is confirmed by solving the NLSE, see Fig. 7(b). In Figs. 8(a) and 9(a) we plot the NGO amplitude predictions for the cases $m=2$ and 4, respectively. In both cases, in accordance with the NGO ray analysis, the beam evolves into a ring structure, as is confirmed by solving the NLSE, see Figs. 8(b) and 9(b).

In general, a ring structure breaks up azimuthally due to modulational instabilities [17]. Therefore, upon further propagation, the ring will evolve to form a ring of filaments. The observation that high-power radially symmetric super-Gaussian input beams initially evolve into a ring structure and subsequently break up into a ring of filaments was confirmed numerically and experimentally in [15,17].

We now ask whether the linear Schrödinger model could produce the same peak and ring formation dynamics. To see that, we present the corresponding solutions of the linear Schrödinger equation. In the case of a Gaussian input beam ($m=1$), the linear solution undergoes initial broadening, see Fig. 7(c). In the case of a soft aperture super-Gaussian input beam ($m=2$), the linear solution has a single peak, see Fig.

FIG. 8. (Color online) Solution of the two-dimensional cubic NLSE with a soft ($m=2$) super-Gaussian input beam from Fig. 6(b). (a) NGO prediction for the amplitude at $z \approx 0.05$. (b) NLSE solution at $z \approx 0.04$. (c) Linear Schrödinger solution at $z \approx 0.027$.
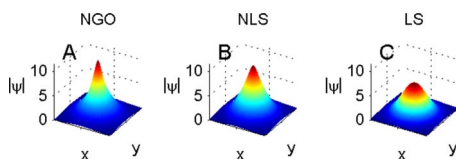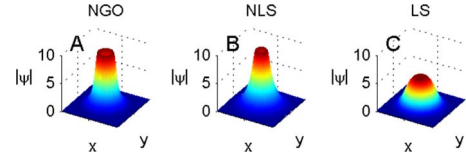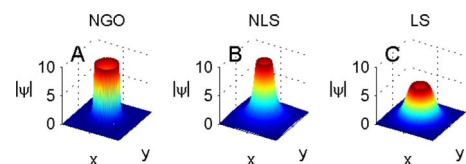

FIG. 7. (Color online) Solution of the two-dimensional cubic NLSE with the Gaussian input beam from Fig. 6(a). (a) NGO prediction for the amplitude at $z \approx 0.04$. (b) NLSE solution at $z \approx 0.026$. (c) Linear Schrödinger solution at $z \approx 0.027$.

FIG. 9. (Color online) Solution of the two-dimensional cubic NLSE with a hard ($m=4$) super-Gaussian input beam from Fig. 6(c) (a) NGO prediction for the amplitude at $z \approx 0.045$. (b) NLSE solution at $z \approx 0.04$. (c) Linear Schrödinger solution at $z \approx 0.027$.
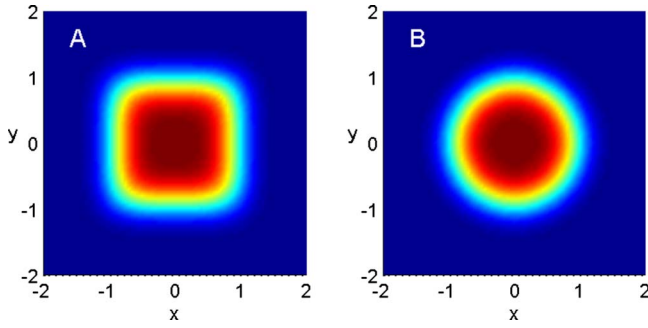
FIG. 10. (Color online) (a) Square profile $\psi = ce^{-x^4 - y^4}$. (b) "Circular" profile $\psi = ce^{-(x^2+y^2)}$.

8(c). Only in the case of a hard aperture super-Gaussian input beam ($m=4$), the linear solution evolves into a ring, see Fig. 8(c). Therefore Observation III.2 that the linear Schrödinger equation predicts the initial self-focusing dynamics only when the input beam propagates through hard apertures is also valid for the two-dimensional radially symmetric case.

B. Square input beams

We now consider the two-dimensional NLSE (27) with collimated input beams of the form

$$\psi_0 = ce^{-x^{2m}}e^{-y^{2m}}, \tag{31}$$

where c is sufficiently large so that Kerr nonlinearity initially dominates diffraction. When $m > 1$, these input beams will be denoted as *square beams*, since the profiles are "square" in the (x,y) plane, see, e.g., Fig. 10(a). This is in contrast with a Gaussian beam ($m=1$), which is a "circle" in the (x,y) plane, see Fig. 10(b).

In this case, by Eq. (22), the corresponding equation for the trajectories of the rays and for the amplitude evolution is given by

$$\frac{d}{dz}(x(z),y(z),A(z))$$
$$= 2c^2 z \left(\frac{\partial}{\partial x}, \frac{\partial}{\partial y}, -\frac{1}{2} A \left[\frac{\partial^2}{\partial x^2} + \frac{\partial^2}{\partial y^2} \right] \right) e^{-2x^{2m}}e^{-2y^{2m}}. \tag{32}$$

Previously, in Fig. 2 we saw that when $m=2$, the rays localize around the four vertices of a square and the input beam breaks into four filaments, see Figs. 2(a) and 2(b). This filamentation dynamics is also observed in the NGO prediction for the amplitude [Figs. 2(c) and 11(a)] and is confirmed by the direct simulations of the two-dimensional NLSE [Fig. 11(b)].

C. One-dimensional building blocks

The splitting into four filaments located on the corners of a square can be explained by considering the dynamics of the x and y components of the input beam (e^{-x^4} and e^{-y^4}) separately. Indeed, in Fig. 4 the NGO method showed that the
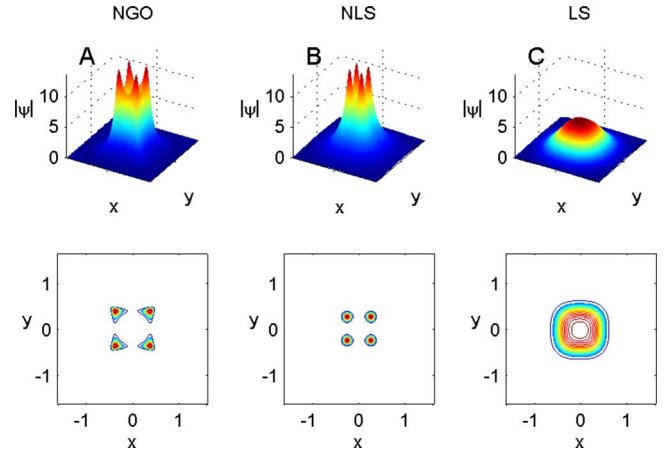

FIG. 11. (Color online) Solution of the two-dimensional cubic NLSE with a square input beam $\psi_0 = ce^{-x^4}e^{-y^4}$ where $c \approx 6.55$. Top: surface plot. Bottom: level sets of $|\psi|$. (a) NGO prediction for the amplitude at $z \approx 0.075$. (b) NLSE solution at $z \approx 0.05$. (c) Linear Schrödinger solution at $z \approx 0.05$.

one-dimensional input beam e^{-x^4} splits into two beams located at $x = \pm a$. The two-dimensional analog of this dynamics is that the beam splits into two vertical strips centered at $x = \pm a$. Likewise, the two-dimensional input beam e^{-y^4} splits into two horizontal stripes centered at $y = \pm a$. The "product" of the vertical stripes around $x = \pm a$ and the horizontal stripes around $y = \pm a$ attains its maximum around the four corners $(\pm a, \pm a)$.

To further illustrate that the filamentation dynamics of square beams can be analyzed using *one-dimensional* "building blocks," we consider the input beam

$$\psi_0 = ce^{-x^4}e^{-y^2},$$

where c is sufficiently large so that Kerr nonlinearity initially dominates diffraction. In this case, the x component e^{-x^4} is expected to split into two vertical stripes, while the y component e^{-y^2} is expected to localize to a single horizontal strip around the center. The "product" of the vertical stripes around $x = \pm a$ and the horizontal stripe around $y = 0$ attains its maximal value around the two peaks at $(\pm a, 0)$. Therefore we expect the beam to split in the x direction into two localized beams. Indeed, this splitting is observed in Fig. 12(a) where we plot the amplitude distribution predicted by the NGO method. This NGO prediction is confirmed by solving the NLSE, see Fig. 12(b). Therefore it is possible to analyze the filamentation dynamics of square beams using one-dimensional "building blocks."

We can also use one-dimensional building blocks to analyze the filamentation dynamics of *rectangular beams*. For example, consider the input beam $\psi_0 = ce^{-x^4}e^{-4y^4}$. In this example, under the rescaling $y \to y/\sqrt{2}$, the input beam becomes a square input beam of the NLSE

$$i\psi_z(z,x,y) + \psi_{xx} + 2\psi_{yy} + |\psi|^2\psi = 0. \tag{33}$$

Hence the x component e^{-x^4} splits into two vertical stripes, the y component e^{-y^2} splits into two horizontal stripes, and
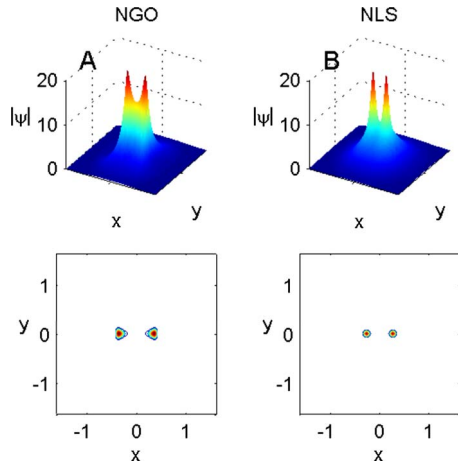
FIG. 12. (Color online) Solution of the two-dimensional cubic NLSE with the input beam $\psi_0 = ce^{-x^4}e^{-y^2}$ where $c \approx 7.23$. Top: surface plot. Bottom: level sets of $|\psi|$. (a) NGO prediction for the amplitude at $z = 0.08$. (b) NLSE solution at $z \approx 0.049$.

their "product" attains its maximal value around four localized peaks located on the corners of the square $(\pm a, \pm a)$ in the rescaled variables [which in the original variable will be four corners of the rectangle $(\pm a, \pm \sqrt{2}a)$]. However, in the case of the anisotropic NLSE (33), we expect the input beam to first split in the y direction into two vertical stripes which are each nearly uniform in x, and only later to undergo a second split in x into a total of four localized beams. Indeed, in Fig. 13(a) we plot the NGO prediction for the amplitude distribution of the solution and observe that the beam initially splits in the y direction. Subsequently, at longer distances, rectangular beams experience a second split in x into four localized beams at the corners of a rectangle, see Fig. 14(a). This NGO predication is confirmed by solving the NLSE (27), see Figs. 13(b) and 14(b).

D. Generic self-focusing dynamics of square beams

In Sec. V C, we showed that it is possible to analyze the filamentation dynamics of square beams using one-
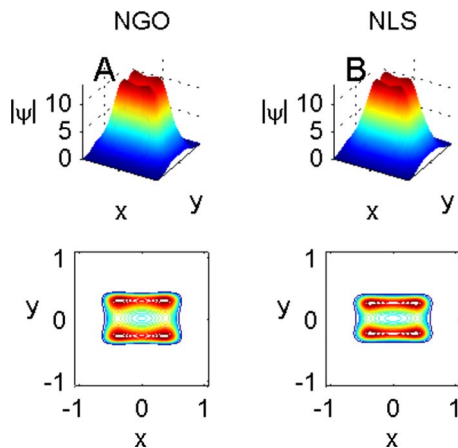

FIG. 13. (Color online) Solution of the two-dimensional cubic NLSE with the input beam $\psi_0 = ce^{-x^4}e^{-4y^4}$ where $c \approx 6.55$. Top: surface plot. Bottom: level sets of $|\psi|$. (a) NGO prediction for the amplitude at $z = 0.02$. (b) NLSE solution at $z \approx 0.016$.
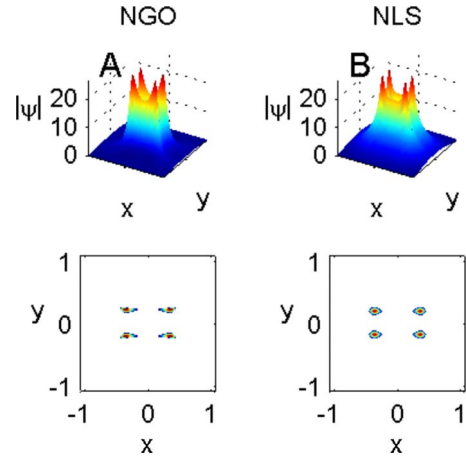

FIG. 14. (Color online) Same as Fig. 13. (a) NGO prediction at $z = 0.07$. (b) NLSE solution at $z \approx 0.024$.

dimensional "building blocks." Therefore Observation (III.1) for the one-dimensional super-Gaussian "building blocks" implies that

Observation V.2. Any two-dimensional square input beam with $m > 1$, whose power is sufficiently high so that initially the Kerr nonlinearity dominates over diffraction, will split into four filaments located on the corners of a square.

To confirm this observation, we consider the case of a high-power square input beam with $m = 4$. As expected, in this case the NGO solution breaks up into four filaments located on the corners of a square, see Fig. 15(a). This prediction is confirmed by solving the two-dimensional NLSE directly, see Fig. 15(b).

We note that Roskey *et al.* also studied numerically the filamentation dynamics of square input beams (31) with $m = 4$ [16]. In this case, they were able to predict the filamentation pattern using the linear Schrödinger model, see Fig. 15(c). As already noted, in the linear model the splitting occurs as the beam diffracts, whereas in the NGO method the splitting occurs as the filaments self-focus, as indeed occurs
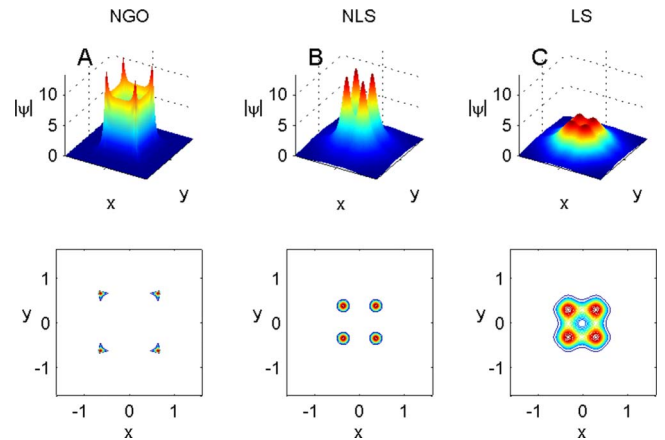

FIG. 15. (Color online) Solution of the two-dimensional cubic NLSE with a square input beam $\psi_0 = ce^{-x^8}e^{-y^8}$ where $c \approx 5.79$. Top: surface plot. Bottom: level sets of $|\psi|$. (a) NGO prediction for the amplitude at $z \approx 0.06$. (b) NLSE solution at $z \approx 0.049$. (c) Linear Schrödinger solution at $z \approx 0.052$.

in the NLSE. In addition, when $m=2$ the NLSE (and NGO) solution breaks up into four filaments on a square, whereas the linear solution has a single peak, see Fig. 11(c). This confirms Observation III.2 for the case of square input beams, namely that the linear model predicts the filamentation dynamics of hard aperture input beams only.

VI. EFFECT OF A LENS

The NGO method developed in Sec II, and its applications that were presented so far, were only for collimated beams. We now analyze the effect of a lens on the filamentation pattern of high-power beams. One possible approach is to extend the NGO method to the case of focused input beams. The resulting equations, however, are not as easy to analyze as in the case of collimated beams, see Appendix C. Therefore, in what follows, we adopt a different approach.

Let us begin with the case of the two-dimensional NLSE (27). The initial condition $\widetilde{\psi}_0$ that corresponds to a collimated input beam ψ_0 which is focused by a lens with focal distance F is given by

$$\widetilde{\psi}_0 = \psi_0(x,y)e^{-i(x^2+y^2)/4F}. \tag{34}$$

In the case of a two-dimensional Kerr medium, the effect of the lens follows from the *lens transformation*, due to Talanov [18], which is as follows. Let $\psi(z,x,y)$ be a solution of the NLSE (27) and let

$$\widetilde{\psi}(z,x,y) = \frac{1}{L(z)}\psi(\zeta,\xi,\eta)e^{iL_z/L(x^2+y^2)/4}, \tag{35a}$$

where

$$L(z) = 1 - \frac{z}{F}, \quad \zeta = \int_0^z \frac{ds}{L^2(s)} = \frac{Fz}{F-z}, \quad \xi = \frac{x}{L(z)}, \quad \eta = \frac{y}{L(z)}. \tag{35b}$$

Then $\widetilde{\psi}$ is also an exact solution of the NLSE.

Since the initial condition for $\widetilde{\psi}$ is given by Eq. (34), the lens transformation shows that the propagation dynamics of $\widetilde{\psi}$ in (z,x,y) is exactly the same as the propagation dynamics of ψ in (ζ,ξ,η). In particular, *the initial filamentation pattern of two-dimensional input beams is unaffected by the lens.* To illustrate this point, we recall that in Fig. 11 we saw a high-power square input beam that collapsed at $z_{fil} \approx 0.055$ into a square of filaments located at $(x=\pm a, y=\pm a)$. In Fig. 16, we repeat this simulation for the same input beam, but which is now focused by a lens with $F=0.0275$. As predicted by the lens transformation, the focused input beam collapses at $\widetilde{z}_{fil} \approx 0.018$ into a square of filaments located at $(x=\pm\widetilde{a}, y=\pm\widetilde{a})$ where $\widetilde{a}=L(z_{fil})a$ and $1/\widetilde{z}_{fil}=1/z_{fil}+1/F$.

$$\widetilde{\psi}_0 = \psi_0(x)e^{-ix^2/4F}. \tag{36}$$

In the case of the one-dimensional NLSE (27) there is no equivalent lens transformation. Intuitively, this is because a focusing lens ($F>0$) increases both the diffraction and the Kerr nonlinearity, but at a different rate. To see that, let us consider the solution in the "lens coordinates," i.e.,
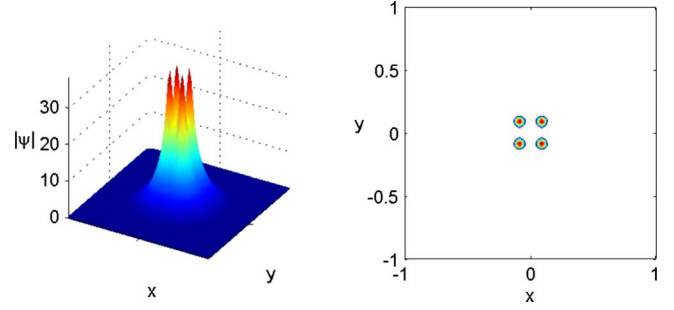

FIG. 16. (Color online) Solution of the two-dimensional cubic NLSE with square beam $\psi_0=ce^{-x^4-y^4}e^{-i(x^2+y^2)/4F}$ where $c\approx6.55$ and $F=0.0275$ at $z\approx0.018$. Left: surface plot. Right: level sets of $|\psi|$.

$$\widetilde{\psi}(z,x) = \frac{1}{\sqrt{L(z)}}\psi(\zeta,\xi)e^{iL_z/Lx^2/4}, \tag{37}$$

where $L(z)$, ζ, and ξ are given by Eq. (35b). The equation for $\widetilde{\psi}$ is

$$i\widetilde{\psi}_z(z,x,y) + \widetilde{\psi}_{xx} + L(z)|\widetilde{\psi}|^2\widetilde{\psi} = 0, \quad L(z) = 1 - \frac{z}{F}. \tag{38}$$

This equation shows that as a result of the focusing lens, the ratio of the nonlinearity over diffraction decreases linearly by $L(z)$. In particular, at the filamentation distance z_{fil}, this ratio decreases by $L(z_{fil})=1-z_{fil}/F$. Therefore there are two limiting cases.

(1) $z_{fil}\ll F$. In this case, $L(z_{fil})\approx1$, hence the propagation dynamics of $\widetilde{\psi}$ in the lens coordinates is essentially the same as that of ψ in the original coordinates. In particular, the lens does not affect the filamentation pattern. To illustrate this point we added a lens with $F=2z_{fil}$ to the super-Gaussian input beam of Fig. 4 and observed that, as in the collimated case, the beam splits into two beams, see Fig. 17(a). Similarly, in Fig. 17(b) we observe that the Gaussian input beam of Fig. 3 with a focusing lens with $F=2z_{fil}$ collapses as a single filament, as in the collimated case.

(2) $F\ll z_{fil}$. In this case, $L(z_{fil})\ll1$. Hence the ratio of the Kerr nonlinearity over diffraction decreases considerably. As a result, the lens can affect the filamentation dynamics. For example, recall that a collimated one-dimensional Gaussian beam self-focuses into a single filament (Fig. 3), whereas
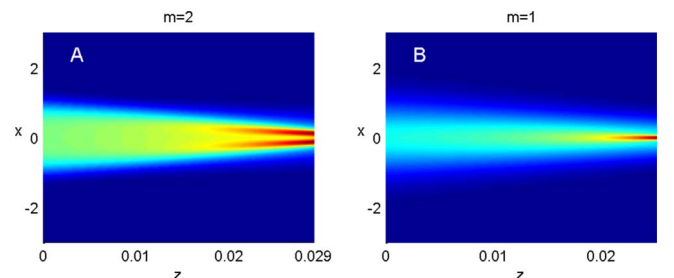

FIG. 17. (Color online) Solution of the one-dimensional cubic NLSE. (a) Super-Gaussian input beam $\psi_0=ce^{-x^4}e^{-ix^2/4F}$ where $c\approx8$ and $F=0.058$. (b) Gaussian input beam $\psi_0=ce^{-x^2}e^{-ix^2/4F}$ where $c\approx9.1$ and $F=0.05$.
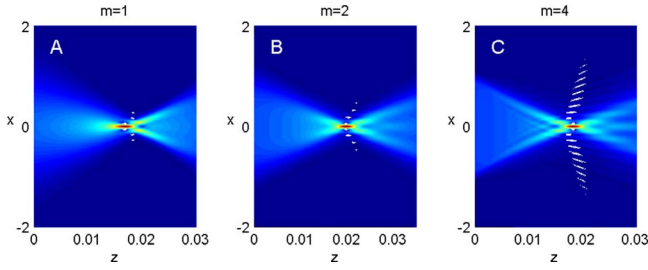
FIG. 18. (Color online) Solution of the one-dimensional cubic NLSE. (a) Gaussian input beam $\psi_0 = ce^{-x^2}e^{-ix^2/4F}$ where $c \approx 9.1$ and $F \approx 0.012$. (b) Super-Gaussian input beam $\psi_0 = ce^{-x^4}e^{-ix^2/4F}$ where $c \approx 8$ and $F \approx 0.014$. (c) Super-Gaussian input beam $\psi_0 = ce^{-x^8}e^{-ix^2/4F}$ where $c \approx 7.5$ and $F \approx 0.013$.

super-Gaussian input beams with $m=2$ and 4 break into two filaments (Figs. 4 and 5). In contrast, when adding a lens with $F = z_{fil}/2$, all three input beams focus into a single filament slightly before the focal point $z = F$, and subsequently split into two beams, see Fig. 18. Therefore the initial filamentation pattern did change because of the lens.

We now ask whether the linear model could predict the filamentation patterns of Fig. 18. To see that, in Fig. 19 we solve the linear Schrödinger equation for the same input beams and observe that all three of them collapse into the focal point as a single filament, but do not split into two filaments after the focal point. Therefore the linear model does not capture the "post focal-point" splitting. Indeed, in these simulations, the ratio of the Kerr nonlinearity over diffraction was initially ≈ 2, and went down to ≈ 1 at the focal point. Therefore the nonlinearity was not negligible at the focal point.

VII. ROBUSTNESS OF THE NGO METHOD

So far we only presented simulations with "clean" Gaussian or super-Gaussians input beams with circular or rectangular profiles. We now illustrate the robustness of the NGO method by applying it to input beams which are closer to the ones in actual experimental setups.

We first consider the two-dimensional cubic NLSE (27) with the asymmetric input beam
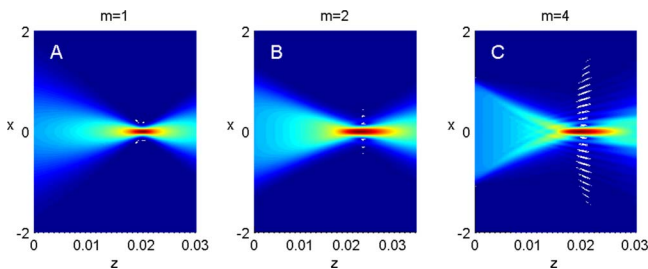

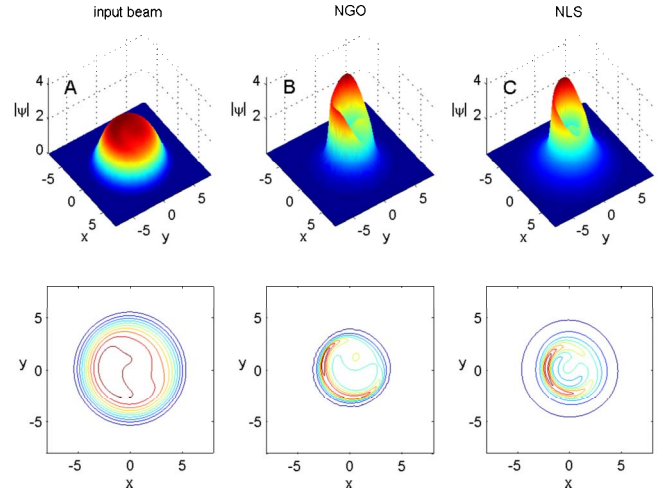FIG. 19. (Color online) Same as Fig. 18 for solutions of the one-dimensional linear Schrödinger equation.

FIG. 20. (Color online) Solution of NLSE with asymmetric input beam (39). Top: surface plot. Bottom: level sets of $|\psi|$. (a) Input pulse. (b) NGO solution at $z=0.825$. (c) NLSE solution at $z=0.06$.

$$\psi_0 = \frac{1}{2} \exp\left[-\frac{x^2 + (y-1)^2}{10} \right]$$
$$- \frac{1}{2} \exp\left[-\frac{[(x-1)^2 + (y-1)^2]^2}{100} \right]$$
$$+ 2 \exp\left[-\frac{(x^2+y^2)^3}{10\,000} \right], \tag{39}$$

which models a flat-top input beam with hot spots, see Fig. 20(a). In this case, the NGO predicts that the beam will evolve into a crestlike shape from which a single filament will emerge, see Fig. 20(b). This filamentation pattern is in agreement with direct simulations of the NLSE, see Fig. 20(c).

Next, we consider a square input beam with phase noise, i.e.,

$$\psi_0 = 8e^{-x^4-y^4}e^{i\varepsilon(x,y)},$$

where the noise $\varepsilon(x,y)$ is uniformly distributed in $[-0.5, 0.5]$, see Fig. 21(a) [21]. Similarly, in Fig. 22(a) we consider a square input beam with an amplitude noise, i.e.,

$$\psi_0 = 8[e^{-x^4-y^4} + \varepsilon(x,y)],$$

where the noise $\varepsilon(x,y)$ is uniformly distributed in $[-0.25, 0.25]$. In both cases, although the noise level is not small, the beams break up into four filaments located on the corners of the square, see Figs. 21(b) and 22(b), as predicted by the NGO method for a clean square input beam, see Fig. 11. Therefore we conclude that the filamentation pattern is relatively insensitive to input beam noise, hence that it can be predicted with the NGO method for a clean input beam. Intuitively, the reason for this is that the diffraction has a smoothing effect, and therefore that noise has a small effect during the initial self-focusing stage. Of course, at very high input powers, the initial filamentation is due to input beam noise (modulation instability) and not due to SPM [4]. At this
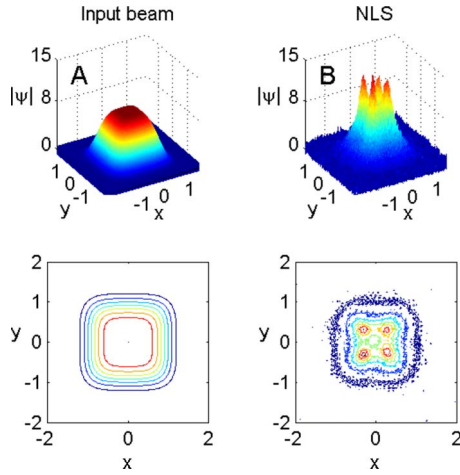
FIG. 21. (Color online) Solution of NLSE with noisy square input beam $\psi_0 = 8e^{-x^4-y^4}e^{i\varepsilon(x,y)}$ where $\varepsilon(x,y)$ is uniformly distributed in $[-0.5, 0.5]$. (a) Input pulse. (b) NLSE solution at $z=0.04$.

high power regime, the NGO method will not predict correctly the filamentation pattern.

VIII. SPATIOTEMPORAL FILAMENTATION

We now consider the propagation of ultrashort laser pulses in a Kerr medium with *anomalous* dispersion, which is modeled by the dimensionless three-dimensional NLSE

$$i\psi_z(z,x,y,t) + \psi_{xx} + \psi_{yy} - \beta\psi_{tt} + |\psi|^2\psi = 0, \quad \beta < 0. \tag{40}$$

Although this equation is not derived from the nonlinear Helmholtz equation (2), it can still be analyzed using the NGO method. This is because, mathematically, we can derive the three-dimensional NLSE (40) from a four-dimensional Helmholtz-like equation.

A. Pulses in waveguide slabs

The propagation of ultrashort laser pulses in waveguide slabs in a Kerr medium with *anomalous* dispersion is modeled by the dimensionless two-dimensional NLSE

$$i\psi_z(z,x,t) + \psi_{xx} - \beta\psi_{tt} + |\psi|^2\psi = 0, \quad \beta < 0. \tag{41}$$

Up to the change $t \leftrightarrow y$, this is the same equation as in the case of two spatial dimensions. Since this case was already discussed in Sec. V B [see Eq. (27) for the case $\beta=-1$ and Eq. (33) for the case $\beta \neq -1$] and since similar examples of spatiotemporal pulses will be discussed in Secs. VIII B and VIII D, we will not further discuss this case.

B. Spherical spatiotemporal input pulses

Under the rescaling $t \to \sqrt{|\beta|}t$, the NLSE (40) becomes

$$i\psi_z(z,x,y,t) + \nabla_\perp^2 + |\psi|^2\psi = 0, \quad \nabla_\perp^2 = \psi_{xx} + \psi_{yy} + \psi_{tt}. \tag{42}$$

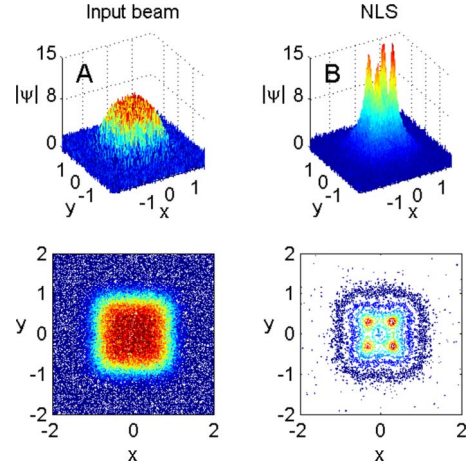Let us consider spherically symmetric input pulses of the form

FIG. 22. (Color online) Solution of two-dimensional cubic NLSE with noisy square input beam $\psi_0 = 8[e^{-x^4-y^4} + \varepsilon(x,y)]$ where $\varepsilon(x,y)$ is uniformly distributed in $[-0.25, 0.25]$. (a) Input pulse. (b) NLSE solution at $z=0.04$.

$$\psi_0(x,y,t) = ce^{-\rho^{2m}}, \quad \rho = \sqrt{x^2 + y^2 + t^2}, \tag{43}$$

where c is set such that $|\psi_0|^2\psi_0 \gg \nabla_\perp^2\psi_0$. In this case, by Eq. (22), the corresponding equation for the ray trajectories is given by

$$\frac{d}{dz}\rho(z) = 2c^2z\frac{\partial}{\partial\rho}e^{-2\rho^{2m}}. \tag{44}$$

Therefore, up to the change $\rho \leftrightarrow x$, this is the same equation as for the ray trajectories in the one-dimensional case, see Eq. (25). In addition, the NGO prediction for the amplitude is given by

$$\frac{dA(z)}{dz} = -c^2zA(z)\left[\frac{\partial}{\partial\rho^2} + \frac{2}{\rho}\frac{\partial}{\partial r}\right]e^{-2\rho^{2m}}. \tag{45}$$

Hence the equation for the amplitude is similar, but not identical, to the one in the one-dimensional case, see Eq. (25). Therefore, as in the one-dimensional case, we expect the input beam to split in ρ. Note that a split in ρ is equivalent to a spherical shell formation in the (x,y,t) plane. Therefore

Observation 8.1. Any three-dimensional spherically symmetric spatiotemporal super-Gaussian input beam with $m > 1$ whose peak power is sufficiently high so that initially the Kerr nonlinearity dominates over diffraction and anomalous dispersion, will initially evolve into a spherical spatiotemporal shell.

In Fig. 23 we consider the three-dimensional NLSE (40) with the spatiotemporal super-Gaussian input pulses (43) with $m=2$. As predicted by the NGO ray analysis, the initial spatiotemporal sphere evolves into a spherical shell, see Fig. 23(a). This prediction is confirmed by direct simulations of the three-dimensional cubic NLSE (42), see Fig. 23(b).

The above results agree with previous theoretical studies which showed that clean three-dimensional super-Gaussian input pulses collapse with a self-similar *shell* profile [19,20]. However, as a shell profile is unstable under azimuthal perturbations, it will break into a shell of spatiotemporal wave
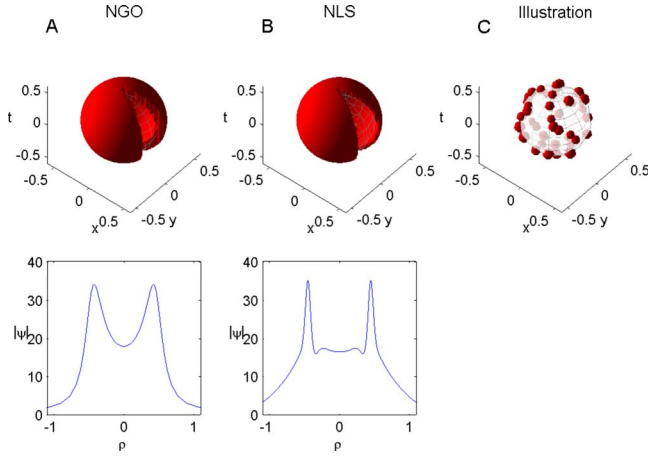
FIG. 23. (Color online) Iso-amplitude plot of the solution of the three-dimensional cubic NLSE with the input pulse $\psi_0 = ce^{-\rho^4}$ where $c \approx 17.8$. Top: surface plot. Bottom: level sets of $|\psi|$. (a) NGO prediction at $z = 0.025$ (max $|\psi| \approx 34$). (b) NLSE solution at $z = 0.02$ (max $|\psi| \approx 32$). (c) Illustration of subsequent filamentation dynamics. In (a) and (b) a portion of the shell was removed for the graphical presentation.

packets. This is similar to the breakup of spatial rings into rings of filaments, see, e.g., Ref. [15], Fig. 33 or Ref. [17], Fig. 23]. Observing the breakup of a spherical shell numerically is demanding, as it requires solving the NLSE in (3 +1) dimensions with no symmetry. Therefore we only present a schematic illustration of breakup into a spatiotemporal wave packets shell in Fig. 23(c).

C. Cylindrical spatiotemporal input pulses

We now consider high-power input pulses of the form

$$\psi_0(x, y, t) = ce^{-r^{2m} - t^{2n}}, \quad r = \sqrt{x^2 + y^2}. \quad (46)$$

These input pulses have a spatiotemporal cylinderlike shape, see top of Fig. 24(a), and have a square profile in the (r, t) plane, see bottom of Fig. 24(a).

For simplicity, we first consider the case $\beta = -1$ in which the coefficient of ψ_{tt} in the three-dimensional NLSE (40) is one as the coefficients of ψ_{xx} and ψ_{yy}, i.e., when the dispersion length is equal to the diffraction length. In this case, by Eq. (22), the corresponding equation for the ray trajectories is given by

$$\frac{d}{dz}(r(z), t(z)) = 2c^2 z \left(\frac{\partial}{\partial r}, \frac{\partial}{\partial t} \right) e^{-2r^{2m} - 2t^{2n}}. \quad (47)$$

Therefore up to the changes $r \leftrightarrow x$ and $t \leftrightarrow y$, Eq. (47) is exactly as Eq. (29) for the two-dimensional square input beam (31). In addition, the NGO prediction for the amplitude is given by

$$\frac{dA(z)}{dz} = -c^2 z A(z) \left[\frac{\partial}{\partial r^2} + \frac{1}{r} \frac{\partial}{\partial r} + \frac{\partial}{\partial t^2} \right] e^{-2r^{2m} - 2t^{2n}}. \quad (48)$$

Hence the equation for the amplitude is similar but not identical to the one in the two-dimensional case, see Eq. (32).
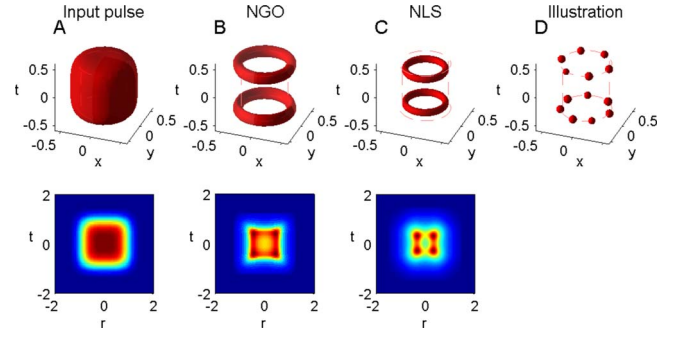

FIG. 24. (Color online) Amplitude of the solution of the three-dimensional cubic NLSE with input pulse $\psi_0 = ce^{-r^4 - t^4}$ where $c \approx 7.1$. Top: Surface plot in (x, y, t) space. Bottom: Amplitude distribution in the (r, t) plane. (a) Input beam. (b) NGO prediction at $z = 0.05$ (max $|\psi| \approx 11$). (c) NLSE solution at $z \approx 0.039$ (max $|\psi| \approx 11.6$). (d) Illustration of later filamentation dynamics.

Therefore as in the case of square input beams in the (x, y) plane (see, e.g., Fig. 11) we expect that when $m, n > 1$, the input beam (46) will split into four "filaments" in the (r, t) plane [see, e.g., bottom of Fig. 24(b)]. Since a split in the r direction corresponds to a tube formation in (x, y, t) space, a beam split in both the r direction and the t direction corresponds to the formation in the (x, y, t) space of two pulses, each of which is a spatial ring. Hence

Observation 8.2. Any three-dimensional cylindrically symmetric spatiotemporal super-Gaussian input pulse with $m > 1$ whose peak power is sufficiently high so that initially the Kerr nonlinearity dominates over diffraction and dispersion, will evolve into two pulses, each of which is a spatial ring.

This prediction is confirmed by direct NLSE simulations, see Fig. 24(c).

Recall that, in general, a ring structure is modulationally unstable [17]. Therefore, upon further propagation, each of the rings in Fig. 24(b) will break into spatiotemporal wave packets. Observing the breakup of the rings numerically is demanding as it requires solving the three-dimensional NLSE with high-accuracy. Instead, we present a schematic illustration of the two rings of spatiotemporal wave packets, see Fig. 24(d).

The example in Fig. 24 shows that it is possible to explain the filamentation dynamics of cylindrical input pulses using the one-dimensional building blocks e^{-r^m} and e^{-t^m}. We can also use these one-dimensional building blocks to analyze the filamentation dynamics of the input beam

$$\psi_0 = ce^{-r^2} e^{-t^4},$$

where c is set such that Kerr nonlinearity initially dominates diffraction and dispersion, see Fig. 25(a). In this case, the r component e^{-r^2} is expected to localize to a single peak, while the t component e^{-t^4} is expected to split in time into two pulses. The "product" of these two profiles is given by two temporally separated spatiotemporal wave packets, see Fig. 25(b). This NGO prediction is confirmed by direct NLSE simulations, see Fig. 25(c).
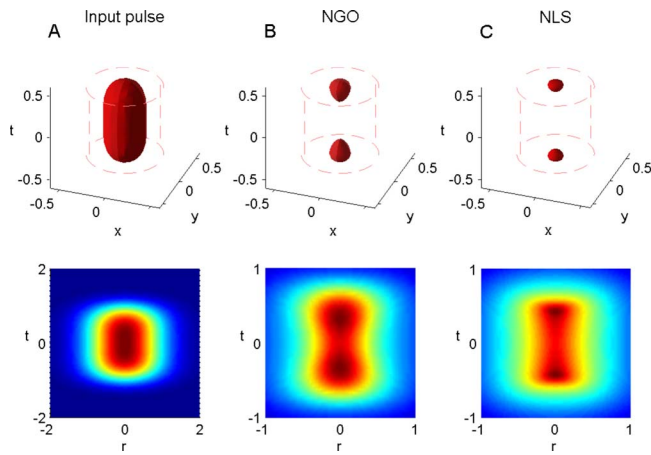
FIG. 25. (Color online) Iso-amplitude plot of the amplitude of the solution of the three-dimensional cubic NLSE with input pulse $\psi_0 = c e^{-r^2 - t^4}$ where $c = 20$. Top: surface plot. Bottom: level sets of $|\psi|$. (a) Input beam. (b) NGO prediction at $z = 0.04$ (max $|\psi| \approx 31$). (c) NLSE solution at $z \approx 0.01$ (max $|\psi| \approx 30$).

We now consider the more general case $\beta \neq -1$ in Eq. (40). This case is similar to the two-dimensional anisotropic NLSE (33). Therefore the same arguments show that when $\beta < -1$, the pulse will first split in time into two pulses, each of which has a spatial disk profile, see Fig. 26(a). Subsequently, each spatial disk will evolve into a spatial ring, see Fig. 27(a). This NGO prediction is confirmed in direct simulations of the NLSE, see Figs. 26(b) and 27(b). Similarly, when $\beta > -1$, the pulse first evolves into a tube which is
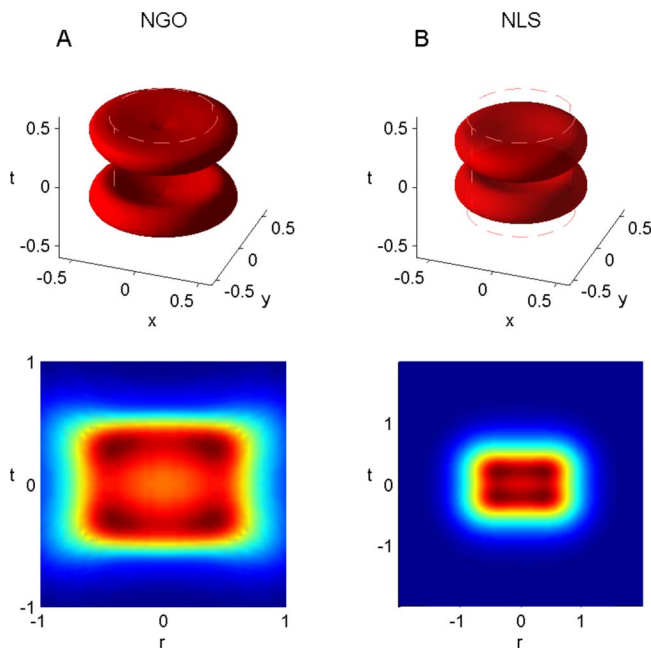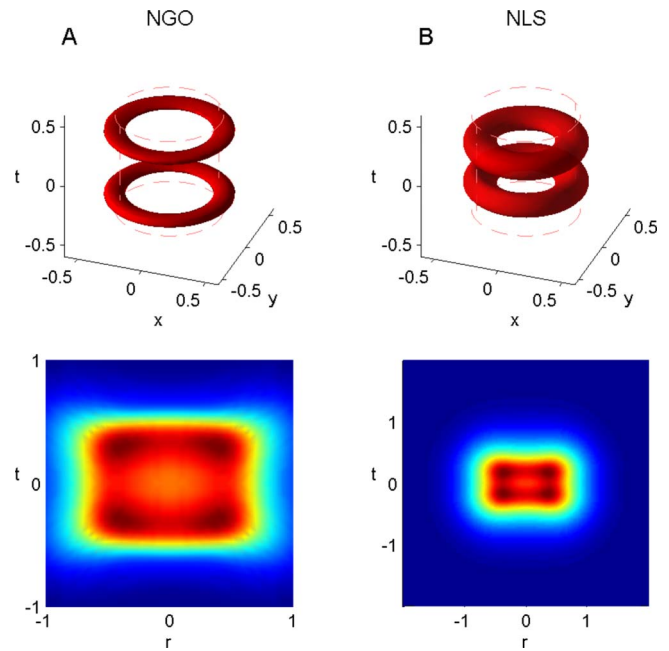

FIG. 27. (Color online) Same as Fig. 26. (a) NGO prediction at $z = 0.05$ (max $|\psi| \approx 10$). (b) NLSE solution at $z \approx 0.033$ (max $|\psi| \approx 9$).

nearly constant in time, see Fig. 28(a). Subsequently, the tube will split in time into two shorter pulses each of which has a ring profile, see Fig. 29(a). This NGO prediction is confirmed in direct simulations of the NLSE, see Figs. 28(b) and 29(b).
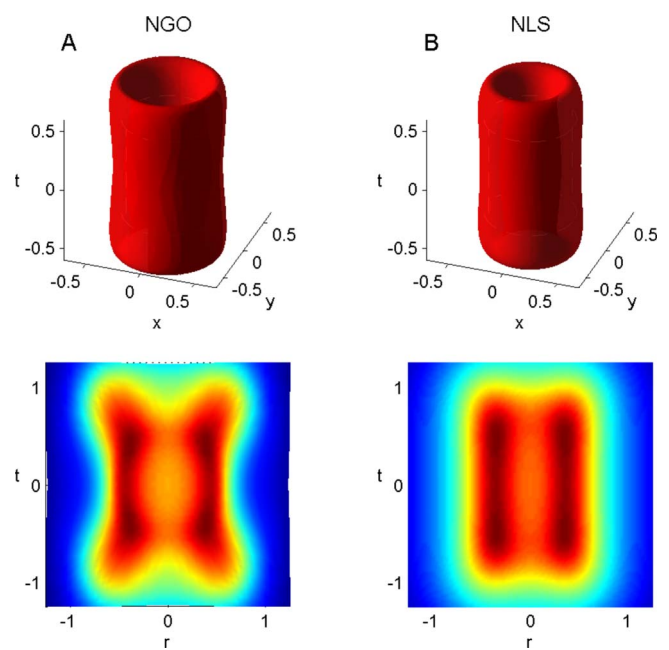

FIG. 26. (Color online) Iso-amplitude plot of the amplitude of the solution of the three-dimensional cubic NLSE with input pulse $\psi_0 = c e^{-r^4 - 4t^4}$ where $c = 7.1$. Top: surface plot. Bottom: level sets of $|\psi|$. (a) NGO prediction at $z = 0.035$ (max $|\psi| \approx 9.5$). (b) NLSE solution at $z \approx 0.02$ (max $|\psi| \approx 8$).

FIG. 28. (Color online) Iso-amplitude plot of the amplitude of the solution of the three-dimensional cubic NLSE with input pulse $\psi_0 = c e^{-r^4 - t^4/4}$ where $c = 7.1$. Top: surface plot. Bottom: level sets of $|\psi|$. (a) NGO prediction at $z = 0.05$ (max $|\psi| \approx 10$). (b) NLSE solution at $z \approx 0.033$ (max $|\psi| \approx 9$)
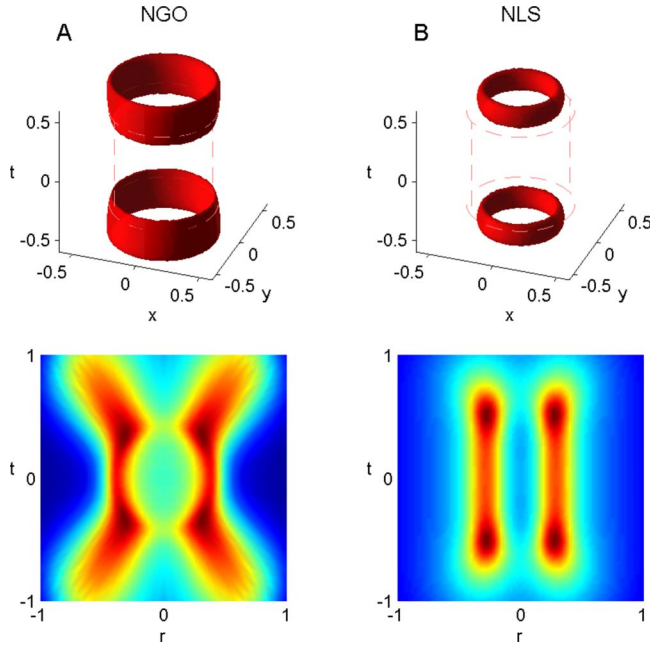
FIG. 29. (Color online) Same as Fig. 28. (a) NGO prediction at $z=0.075$ (max$|\psi|\approx 15$). (b) NLSE solution at $z\approx 0.047$ (max$|\psi| \approx 13$).

D. Spatiotemporal cubic input pulses

Finally, we consider high-powered input pulses of the form

$$\psi_0 = ce^{-x^{2m}-y^{2m}-t^{2n}}, \tag{49}$$

which are a spatiotemporal cube in space time [Fig. 30(a)] when $m,n>1$.

In this case, by Eq. (22), the NGO equation for the ray trajectories is given by

$$\frac{d}{dz}(x(z),y(z),t(z)) = 2c^2z\left(\frac{\partial}{\partial x},\frac{\partial}{\partial y},\frac{\partial}{\partial t}\right)e^{-2x^{2m}-2y^{2m}-2t^{2n}}. \tag{50}$$

The NGO prediction for the amplitude is given by

$$\frac{dA(z)}{dz} = -c^2zA(z)\left[\frac{\partial}{\partial x^2} + \frac{\partial}{\partial y^2} + \frac{\partial}{\partial t^2}\right]e^{-2x^{2m}-2y^{2m}-2t^{2n}}. \tag{51}$$
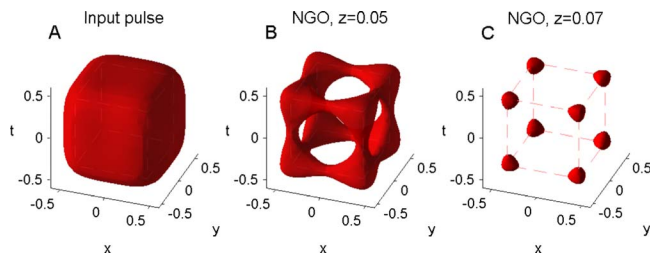

FIG. 30. (Color online) Iso-amplitude plot of the solution of NGO amplitude prediction for input pulse $\psi_0=ce^{-x^4-y^4-t^4}$ where $c \approx 6.5071$. (a) Input pulse. (b) NGO prediction for the amplitude at $z=0.05$. (c) NGO prediction for the amplitude at $z=0.07$.

The cubic input pulses are the three-dimensional analog of square input beams (31), see Sec. V B. Similarly to square input beams, we can use the one-dimensional building blocks $e^{-x^{2m}}$, $e^{-y^{2m}}$, and $e^{-t^{2n}}$ to predict the filamentation dynamics of these input pulses. For example, consider the cubic input pulse $\psi_0=ce^{-x^4-y^4-t^4}$. Recall that each one-dimensional input beam e^{-x^4}, e^{-y^4}, and e^{-t^4} splits into two components centered at $x=\pm a$, $y=\pm a$, and $t=\pm a$, respectively. The "product" of these building blocks attains its maximum around the eight corners ($x=\pm a$, $y=\pm a$, $t=\pm a$). Solving the NGO equations shows that the pulse intensity gradually shifts from the interior of the cube towards its corners [Fig. 30(b)], so that eventually the pulse splits into eight spatiotemporal wave packets, located at the corners of a cube [Fig. 30(c)].

IX. COMPARISON WITH THE LINEAR POWER PARTITIONING METHOD

Recently, Roskey *et al.* [16] presented a linear power partitioning (LPP) method for predicting the filamentation pattern by solving the linear Schrödinger equation and then inspecting the power partitioning. In general, the LPP method is applicable in the weakly nonlinear regime, i.e., when diffraction is dominant over the Kerr effect during the initial filamentation dynamics, whereas the NGO method is applicable in the strongly nonlinear regime, i.e., when the Kerr effect is dominant over diffraction during the initial filamentation dynamics. Surprisingly, however, in certain cases the qualitative predictions of the two methods agree. For example, we saw that the square beam $\psi_0=ce^{-x^8}e^{-y^8}$ will split into four filaments located on the square corners both in the linear regime and in the strongly nonlinear regime.

A comparison between the two methods shows that the NGO method has the following advantages over the LPP method in the strongly nonlinear regime, i.e., when $\nabla^2_\perp \psi_0 \ll |\psi_0|^2\psi_0$,

(1) The LPP method predicts the filamentation pattern correctly only when the input beam has sharp gradients. Thus, for example, the NGO method predicts that high-power square beams $\psi_0=ce^{-x^{2m}}e^{-y^{2m}}$ will split into four filaments for any $m>1$, as is confirmed by direct simulations of the NLSE. The LPP method predicts correctly this filamentation pattern for $m=4$, but not for $m=2$.

(2) Even when the LPP method predicts correctly the filamentation pattern, in the linear model the beam split into filaments occurs as the beam diffracts, while in the NLSE (and in the NGO method) the splitting occurs as the filaments self-focus. Therefore, unlike the NGO method, the linear method does not predict correctly the evolution of the beam amplitude.

(3) Both methods do not accurately predict the filamentation distance. However, in the NGO method the predicted filamentation distance is always somewhat larger than the NLSE filamentation distance. In contrast, the filamentation distance in the linear model is independent of the input power. In particular, unlike the NGO method, the LPP method does not capture the decrease in the filamentation distance as the input power increases.

Of course, when the propagation dynamics is only weakly nonlinear, the LPP method is superior to the NGO method.

APPENDIX A: DERIVATION OF EQ. (13)

In order to write Eq. (1a) in the dimensionless form (12), we introduce the dimensionless variables

$$\tilde{x} = \frac{x}{r_0}, \quad \tilde{y} = \frac{y}{r_0}, \quad \tilde{z} = \frac{z}{2k_0 r_0^2}, \quad \tilde{F} = k_0^2 r_0^2 F(|\psi|^2). \quad \text{(A1)}$$

Let us write the dimensionless NLSE solution as $\tilde{\psi}(z,x,y) = \tilde{A}(\tilde{z},\tilde{x},\tilde{y}) e^{iS_{\tilde{\psi}}(\tilde{z},\tilde{x},\tilde{y})}$. Hence $\tilde{A} = A$ and $S_{\tilde{\psi}} = k_0 S_\psi$. Therefore the dimensionless form of Eq. (9) is given by Eq. (13).

APPENDIX B: MATLAB CODE EXAMPLE FOR THE NGO METHOD

This is an example of a MATLAB code that produces the ray trajectories and amplitude for Fig. 5.

```
% Define rays starting points
rayStartingPoints=linspace(-1.4,1.4,75);zLast=0.05;

for x=rayStartingPoints
  % Find ray trajectory and amplitude along its trajectory
  [z,X] = ode45(@X_ODE,[0,zLast], [x 8.09*exp(-x^8)]);
  % Plot ray trajectory and ampltide change
  hold on;plot3(z,X(:,1),X(:,2));
end
view(-65,25
```

where the MATLAB function X_ODE is defined as

```
  function dXdz=X_ODE(z,X)
  % ODE (9a) for ray trajectory for input beam 8exp(-x^8)
  % solved simultaneously with ODE (10) for change in amplitude
  % along the ray trajectory
  x=X(1);A=X(2);

  % Calculated Gradient and Laplacian of phase
  c=8.09; IC=c*exp(-x^8);
  dx=-16*x^7*IC^2;
  laplacian=16*IC^2*x^6*(16*x^8-7);

  % Calculated vector (dx/dz;dA/dz)
  dXdz=...
    [2*dx*z;...
    -X(2)*laplacian*z];
  return
```

We note that the above code can also be implemented using MATLAB's streamline command. In this case, the MATLAB code may be simpler. However, the generalization of the NGO method to three-dimensions is not possible using the streamline command.

APPENDIX C: EFFECT OF A LENS

We now consider the effect of a lens on filamentation dynamics. In the case of low power input beams, i.e., when self-phase modulation is negligible, the rays are the lines emanating from the focal point $(x=0, z=F)$. Therefore the Helmholtz phase in this case is

$$S_E = -\rho, \quad \rho = \sqrt{x^2 + (z-F)^2}. \quad \text{(C1)}$$

In this case, S_E is the exact solution of the corresponding Eikonal equation $\boldsymbol{\nabla}S \cdot \boldsymbol{\nabla}S = 1$. We now want to find the Helmholtz phase when self-phase modulation is small, but not negligible, so that the corresponding Eikonal equation is $\boldsymbol{\nabla}S \cdot \boldsymbol{\nabla}S = 1 + \varepsilon|\psi_0|^2$.

Let us look for a phase of the form

$$S_E = -\rho + \varepsilon f(x,z).$$

Then,

$$\nabla S_E \cdot \nabla S_E = 1 - 2\varepsilon \, \nabla \rho \cdot \nabla f + O(\varepsilon^2).$$

Balance of the $O(\varepsilon)$ terms gives that

$$-\nabla \rho \cdot \nabla f = \frac{1}{2}|\psi_0|^2, \quad f(x, z = 0) = 0. \tag{C2}$$

This is a linear equation, which can be solved using the method of characteristics. Its exact solution is

$$f(x,z) = -\frac{1}{2}\frac{\rho}{x}\int_{x/L(z)}^{x}|\psi_0(s)|^2 ds, \quad L(z) = 1 - \frac{z}{F}.$$

The Eikonal equations become

$$\frac{dz(\sigma)}{d\sigma} = S_z = \frac{F-z}{\rho}\left[1 - \frac{\varepsilon}{2x}\int_{x/L(z)}^{x}|\psi_0|^2 ds\right]$$

$$+ \frac{\varepsilon}{2}\frac{\rho}{L^2(z)F}|\psi[x/L(z)]|^2,$$

$$\frac{dx(\sigma)}{d\sigma} = S_x = -\frac{x}{\rho} + \frac{\varepsilon}{2}\frac{(F-z)^2}{\rho x^2}\int_{x/L(z)}^{x}|\psi_0|^2 ds$$

$$+ \frac{\varepsilon}{2}\frac{\rho}{x}\{L^{-1}(\bar{z})|\psi_0[x/L(z)]|^2 - |\psi_0(x)|^2\}. \tag{C3}$$

This equation is not as easy to analyze as in the case of collimated beams, see Eq. (22).

---

[1] G. Fibich and A. Gaeta, Opt. Lett. **25**, 335 (2000).

[2] Y. Shen, Prog. Quantum Electron. **4**, 1 (1975).

[3] V. Bespalov and V. Talanov, Zh. Eksp. Teor. Fiz. Pis'ma Red. **3**, 471 (1966) [JETP Lett. **3**, 307 (1966)].

[4] G. Fibich, S. Eisenmann, B. Ilan, Y. Erlich, M. Fraenkel, Z. Henis, A. L. Gaeta, and A. Zigler, Opt. Express **13**, 5897 (2005).

[5] G. Fibich and B. Ilan, Opt. Lett. **26**, 840 (2001).

[6] G. Fibich and B. Ilan, Physica D **157**, 112 (2001).

[7] A. Dubietis, E. Gaižauskas, G. Tamošauskas, and P. DiTrapani, Phys. Rev. Lett. **92**, 253903 (2004).

[8] G. Fibich, S. Eisenmann, B. Ilan, and A. Zigler, Opt. Lett. **29**, 1772 (2004).

[9] G. Mechain, A. Couairon, M. Franco, B. Prade, and A. Mysyrowicz, Phys. Rev. Lett. **93**, 035003 (2004).

[10] A. Dubietis, G. Tamošauskas, G. Fibich, and B. Ilan, Opt. Lett. **29**, 1126 (2004).

[11] P. Rohwetter, M. Queiszer, K. Stelmaszczyk, M. Fechner, and L. Wöste, Phys. Rev. A **77**, 013812 (2008).

[12] M. Centurion, Y. Pu, M. Tsang, and D. Psaltis, Phys. Rev. A **71**, 063811 (2005).

[13] V. P. Kandidov, N. Akzbek, M. Scalora, O. G. Kosareva, A. V. Nyakk, Q. Luo, S. A. Hosseini, and S. L. Chind, Quantum Electron. **34**, 879 (2004).

[14] H. Schroeder, J. Liu, and S. Chin, Opt. Express **12**, 4768 (2004).

[15] T. D. Grow, A. A. Ishaaya, L. T. Vuong, A. Gaeta, N. Gavish, and G. Fibich, Opt. Express **14**, 5474 (2006).

[16] D. Roskey, M. Kolesik, J. V. Moloney, and J. M. E. Wright, Appl. Phys. B: Lasers Opt. **86**, 249 (2007).

[17] G. Fibich, N. Gavish, and X. Wang, Physica D **211**, 193 (2005).

[18] V. Talanov, JETP Lett. **11**, 199 (1970).

[19] G. Fibich, N. Gavish, and X. Wang, Physica D **231**, 55 (2007).

[20] L. M. Degtiarev, V. E. Zakharov, and L. I. Rudakov, Sov. Phys. JETP **41**, 57 (1975).

[21] The addition of phase noise models, e.g., the case when the input profile is shaped using a SLM device.